Received: 13 February 2024 | Revised: 27 June 2024 | Accepted: 16 July 2024

DOI: 10.1111/jace.20062

Journal of the American Ceramic Society

RESEARCH ARTICLE

Precursor impurity-mediated effect in the photocatalytic activity of precipitated zinc oxide

A. M. Ilyas[1] | **Jamal-Deen Musah**[2,3] | **Siu Wing Or**[2,3] | **Ayodeji Oladiran Awodugba**[4]

[1]Hong Kong Centre for Cerebro-Cardiovascular Health Engineering (COCHE), Hong Kong, China

[2]Department of Electrical and Electronic Engineering, The Hong Kong Polytechnic University, Hong Kong, China

[3]Hong Kong Branch of National Rail Transit Electrification and Automation Engineering Technology Research Center, Hong Kong, China

[4]Faculty of Pure and Applied Science, Ladoke Akintola University of Technology, Ogbomoso, Oyo, Nigeria

Correspondence
Siu Wing Or, Department of Electrical and Electronic Engineering, The Hong Kong Polytechnic University, Hong Kong, China.
Email: eeswor@polyu.edu.hk

Funding information
Innovation and Technology Commission of the Hong Kong Special Administrative Region (HKSAR) Government, Grant/Award Number: K-BBY1

Abstract

Photocatalytic degradation of pollutants using nanoparticles presents a promising method globally. However, effectively harnessing light absorption while mitigating recombination and nanoparticle agglomeration remains challenging. Here, we explore the synthesis and characterization of zinc oxide nanoparticles for photocatalytic dye removal in water. The ZnO catalyst, controlled by impurity amount, is developed, demonstrating a notable impact on photolytic performance. Various zinc precursors, namely, zinc acetate, zinc sulfate, zinc nitrate, and zinc chloride, were used in the precipitation technique. Optical characterization showed distinct band transitions and UV-dominant absorption peaks, indicating the presence of different impurities in each precursor. Photocatalytic performance is assessed using Rhodamine B decomposition with the sample prepared from zinc acetate, demonstrating enhanced photocatalytic activity attributed to its larger surface area, surface defects, and superior morphology, enabling efficient organic pollutant degradation. Oxygen vacancies aid in charge carrier separation, crucial for effective photocatalysis. The material's intense interaction with pollutants and a high photocurrent density of 5.18 μAcm^{-2} highlight superior electron–hole pair separation capabilities influenced by morphology and impurity-generated defects, significantly boosting its overall photocatalytic reaction. These findings emphasize the critical role of precursor selection in designing effective ZnO-based photocatalysts, water treatment, and environmental remediation applications.

KEYWORDS
photocatalytic dye, precursor selection, Rhodamine B decomposition, water purification, zinc oxide nanoparticles

A. M. Ilyas and Jamal-Deen Musah have equal contribution.

1 | INTRODUCTION

Industrial evolution has created a lot of negative environmental influences, such as water pollution due to careless release of waste products into water bodies and drainage systems. The use of solar energy-assisted semiconductor processes known as photocatalysis in removing contaminants like dye has been an area of focus.[1,2] Oxide semiconductors, such as zinc oxide (ZnO), niobium oxide (Nb_2O_5), cuprous oxide, titanium oxide (TiO_2), and tin oxide (SnO_2), have attracted a lot of interest in this photocatalytic application. Still, ZnO and TiO_2 have been the most prominent. In the photooxidation of organic compounds, ZnO is more efficient than TiO_2.[3] Zinc oxide is a semiconductor activated with UV light during solar application because of its wide energy band gap.[4] It is an excellent material for excitonic devices.[5,6] Its broad chemistry provides versatility for low-threshold optical pumping, wet-chemical etching, and biocompatibility.[7] It has good catalytic, optoelectronic, electrical, and photochemical properties, which make it useful in gas sensing, medicine, varistors, photodetectors, and light-emitting diodes.[8,9] Its chemical and physical properties change depending on its nanostructure morphology. Several different methods have been used to synthesize ZnO on nanoscales, such as hydrothermal methods,[10] laser ablation,[11] sol–gel methods,[12] electrochemical depositions,[13] chemical vapor deposition,[14] combustion method,[15,16] thermal decomposition,[17] coprecipitations,[18] ultrasound,[19] and two-step mechanochemical-thermal synthesis.[20] Precursor inconsistency has been a significant problem in the chemical synthesis of ZnO nanoparticles that require a Zn source. Researchers chose the Zn source without considering the effect of possible impurities precipitated with the end product (ZnO). For example, Bilecka et al.[21] and Hong et al.[22] used zinc acetate, Tseng et al.[23] used chloride precursor, and Wahab et al.[24] and Thirumavalavan et al.[25] used zinc nitrate, whereas Sharma et al.[26] used zinc sulfate.

Numerous scientific investigations have unveiled innovative approaches to designing floating photocatalytic systems by anchoring highly active photocatalysts onto floatable substrates. By facilitating direct interaction with illuminated light and oxygen molecules at the water/air interface, these systems optimize photocatalytic efficiency by generating more reactive species crucial for catalytic reactions.[27] Moreover, the easy retrieval of used photocatalysts for subsequent processes minimizes secondary pollution and operational costs. The study underscored the efficacy of developed floating photocatalysts across various applications and outlined the diverse floating substrates and potential mechanisms involved in their operation. Furthermore, emerging self-floating photocatalytic systems are deliberated upon, combining photothermal and photocatalytic effects to introduce a new class of floating photocatalysts that harness abundant solar energy for water desalination and purification.

Moreover, heterogeneous photocatalysis offers an energy-efficient solution to environmental and energy challenges by suppressing charge recombination. Forming heterojunctions among photocatalyst components enhances charge separation but can disrupt charge transfer.[28] Constructing homojunction within a single semiconductor is a promising alternative, ensuring a well-matched lattice and strong bonding for effective charge migration. With built-in electric fields, this homojunction facilitates efficient charge separation and transfer. Research on emerging homojunction photocatalysts for degrading wastewater pollutants shows excellent potential for improved performance in photocatalytic processes, encouraging further exploration in this field.[28]

Further, it is reported elsewhere[29] that the worldwide issue of antibiotic contamination in aquatic environments has led to research focusing on degrading these persistent compounds. Heterogeneous photocatalysis is being explored as an effective and environmentally friendly method for eliminating these pollutants. Graphitic carbon nitride (g-C_3N_4), a metal-free photocatalyst, has gained attention for its unique properties but faces challenges such as limited visible-light absorption and charge recombination. Researchers are developing g-C_3N_4-based heterojunction systems with compatible semiconductors to address these issues and enhance their photocatalytic performance. By integrating various semiconductors into Z- and S-scheme structures with g-C_3N_4, significant progress has been made in improving the degradation of antibiotics.[29] The study discussed recent advancements in using g-C_3N_4 heterojunction systems for antibiotic removal and outlined future research directions and challenges.

This work investigated the photocatalytic activity of different ZnO samples synthesized from zinc acetate, zinc nitrate, zinc chloride, and zinc sulfate in the degradation of Rhodamine B (RhB) solution.

2 | EXPERIMENTAL SECTION

2.1 | Materials and synthesis

Analytical grades of zinc chloride ($ZnCl_2$), zinc sulphate ($ZnSO_4$), zinc nitrate ($Zn(NO_3)_2 \cdot 4H_2O$), zinc acetate ($Zn(CH_3COO)_2$), and sodium hydroxide (NaOH) used in this study were purchased from Sigma-Aldrich. RhB contaminants were purchased from LAMBDA PKYSIK.

To obtain ZnO, Zn salts (X) were precipitated with sodium hydroxide according to the following equa-

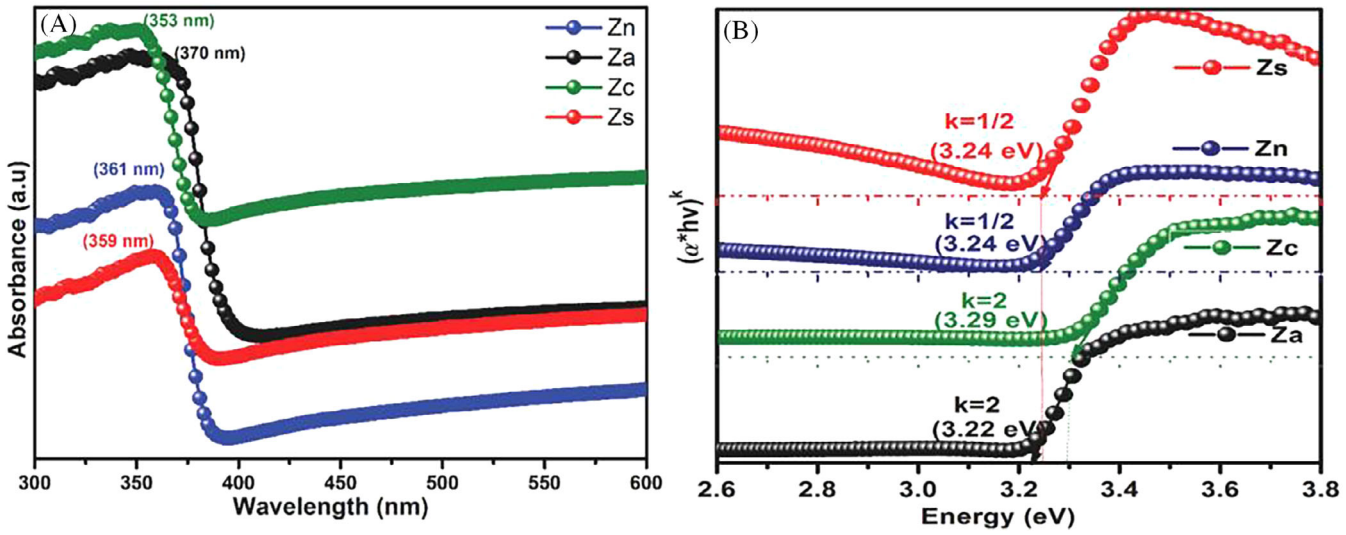

FIGURE 1 (A) Absorbance spectra of the synthesized ZnO samples and (B) Tauc plot used to obtain the band gap of the synthesized ZnO samples.

tion: $X + 2NaOH \rightarrow Zn(OH)_2 + Y$. The precipitates were obtained alongside with $Zn(OH)_2$ represented by Y were $NaNO_3$, NaCl, CH_3COONa, and Na_2SO_4 for $Zn(NO_3)_2 \cdot 4H_2O$, $ZnCl_2$, $Zn(CH_3COO)_2$, and $ZnSO_4$ salts (X), respectively. The precipitate obtained was filtered and washed to remove impurities, and the obtained end product was dried to obtain ZnO nanoparticles. The white precipitate was washed twice with deionized water and ethanol, which is now assumed to be $Zn(OH)_2$, to remove impurities. The samples obtained were labeled Z_s, Z_n, Z_c, and Z_a, which correspond to zinc oxide obtained from zinc sulfate, zinc nitrate, zinc chloride and zinc acetate. ZnO was obtained by drying $Zn(OH)_2$ a 400°C.[30]

2.2 | Material characterization

Bruker advance-D8 diffractometer was used to investigate the crystallization of the prepared ZnO samples, and Jasco 670 double beam spectrophotometer was used to acquire their UV–Vis absorption spectra. The morphology of the samples was obtained with a scanning electron microscope (SEM) (JEOL JSM-6610LV). Fluorolog FL3-iHR, HORIBA Jobin Yvon, using a Xenon lamp light source with 370 nm excitation wavelength, was used to obtain the photoluminescence (PL) property. X-ray photoelectron spectroscopy (XPS) experiments of the ZnO samples were carried out using the ESCALAB-250Xi system (Thermos-Scientific) with Al K_α radiation ($h\upsilon$= 1486.6 eV), and the spectra obtained were analyzed with Avantage software.

2.3 | Photodegradation experiment

Photocatalytic capabilities of ZnO samples were investigated by suspending the synthesized ZnO samples (0.1 g) in 200 mL of RhB solution under an ultraviolet light filter equipped with 500 W Xenon lamp (Oriel). To ensure adsorption equilibrium between the ZnO samples and RhB, the suspension was kept under stirring in the dark for 25 min before exposure to the UV light. The particles were separated from the RhB solution by centrifugation at 4000 rpm, 2 min at regular intervals of 12 min. However, the amount of RhB removed was quantified by measuring the absorption property at 554 nm using UV–Vis spectroscopy (JASCO V-670).

Nitrogen adsorption–desorption measurements were carried out using ChemBET 3000 Instrument to determine the Brunauer–Emmett–Teller (BET) surface area. Before measurement, samples were kept in a desiccator until testing. The ZnO nanoparticles' photoelectrochemical analysis was conducted using the PARSTAT 4000 with a three-electrode configuration. The process involved utilizing the synthesized ZnO nanoparticles on fluorine-doped tin oxide (FTO) substrates as the working electrode, with Pt wire as the counter electrode and Ag/AgCl as the reference electrode. A Xenon arc lamp provided light and a 0.1 M Na_2SO_4 aqueous solution served as the electrolyte. The working electrode preparation included a slurry solution of ZnO photocatalyst, polyethyleneglycol-400, and ethanol coated on the FTO substrate using the doctor-blade method, dried at 300°C for 45 min in a muffle furnace.

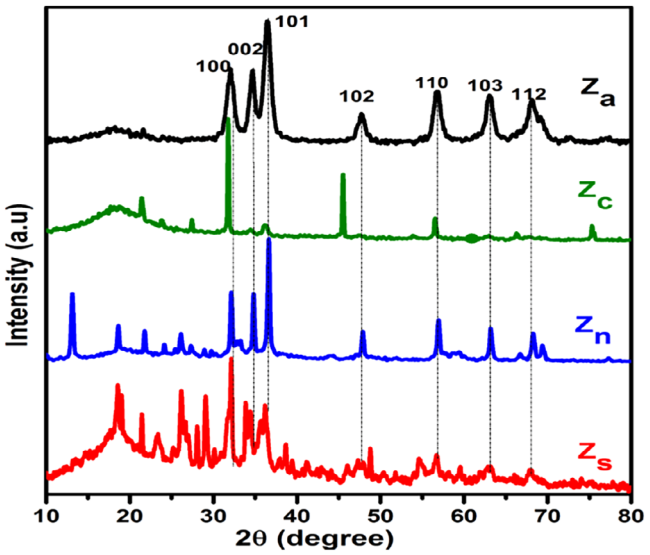

FIGURE 2 X-ray diffraction (XRD) patterns of the synthesized ZnO samples (Z_a, Z_c, Z_n, and Z_{so}).

3 | RESULTS AND DISCUSSION

3.1 | Absorption property

The absorption property of the ZnO samples was determined from the UV–Vis absorption spectra shown in Figure 1A. The absorption peak of the ZnO samples lies in the UV-spectral region at wavelengths of 353, 370, 361, and 359 nm for Z_c, Z_a, Z_n, and Z_s samples, respectively. The absorptions of Z_n, Z_s, and Z_c are found in the deep UV region, whereas that of Z_a is found in the far UV region, which implies that the Z_a sample covers a wider range of the UV spectral region than other samples. The plot of $(\alpha h\upsilon)^k$ vs $h\upsilon$ (where the value of k represents the type of transition) was linearly extrapolated to obtain the band gap of the samples from the absorption spectrum, as shown in Figure 1B. Z_s and Z_n show an indirect ($k = 1/2$) band gap of 3.24 eV, whereas Z_a and Z_c show a direct ($k = 2$) band gap of 3.22 and 3.29 eV, respectively.

3.2 | Structural and morphological analysis

The crystal structure of the synthesized ZnO samples was characterized using the X-ray diffraction (XRD) technique. A typical XRD pattern of the ZnO samples is shown in Figure 2. The diffraction peaks labeled in the pattern are matched with the reported values for ZnO crystal, which has a hexagonal wurtzite structure with lattice constants $a = 3.248$ Å and $c = 5.206$ Å (JCPDS card, No. 36-1451). Discrepancies observed include the appearance of peaks before the significant peaks, which are signatures of precipitates mentioned in the chemical reaction.

There are few or no such extra peaks in the XRD pattern of the Z_a sample, but populated peaks are observed in the Z_s sample. The peak with the highest intensity differs in the samples. The (1 0 1) plane has the highest intensity for Z_a and Z_n samples, but the (1 0 0) plane for Z_s and Z_c samples. The crystal size of the samples has an inverse relationship with the full width at half maximum of the highest peak observed in the XRD pattern according to the Scherrer formula.[31] Therefore, the Z_a sample with the broadest peak has the smallest crystal size (~1.12 nm), and Z_c has the largest crystal size (~4.46 nm). The SEM images of the synthesized ZnO nanoparticles are shown in Figure 3A. It is found that the Z_a sample is composed of interconnected spherically shaped particles, the Z_s sample shows a two-dimensional flat plate appearance, and Z_n shows an irregularly shaped flower-like morphology. In contrast, Z_c shows an interconnected coral creep appearance. Hence, the morphology of the synthesized ZnO samples differs in appearance.

3.3 | Photoluminescence spectra

The radiative recombination of photogenerated electrons and holes generates PL spectra. This measures the charge carrier trapping and transfer efficiency in the semiconductor. The PL spectra obtained from the synthesized Z_a, Z_c, Z_s, and Z_n samples are shown in Figure 3B. The PL results show a broad peak at ~ 555 nm for Z_c and Z_n and ~570 nm for Z_a and Z_s. The broad peak in the visible spectrum region is the superimposition of the yellow and green emissions caused by extrinsic and intrinsic defects due to oxygen vacancy and interstitial oxygen in the ZnO samples. The ZnO samples have different PL emission intensities, the highest in the Z_a sample and the lowest in the Z_n sample. This suggests oxygen defects vary in all the ZnO samples, which play a significant role in the photocatalytic activity.

3.4 | XPS analysis

An XPS analysis of the ZnO samples was done to investigate further the oxidation state of the samples' major elements (Zn and O). The spin–orbit split observed in the Zn 2p peak of the synthesized ZnO samples is compared, and the Zn $2p_{3/2}$ peak is shown in Figure 4. The O1s peak of the ZnO samples is compared and shown in Figure 5. For the Z_a sample, the Zn $2p_{3/2}$ peak was a single peak located

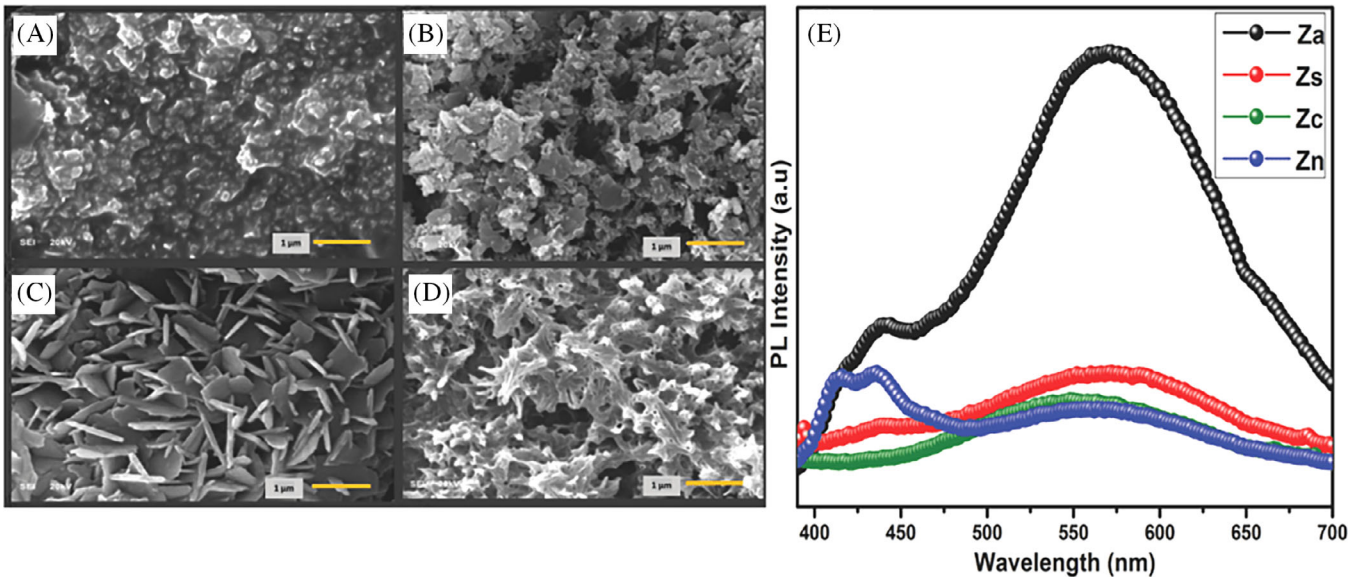

FIGURE 3 The scanning electron microscope (SEM) morphology of all the synthesized samples: (A) Z_a; (B) Z_n; (C) Z_s; (D) Z_c; and (E) photoluminescence (PL) spectra.

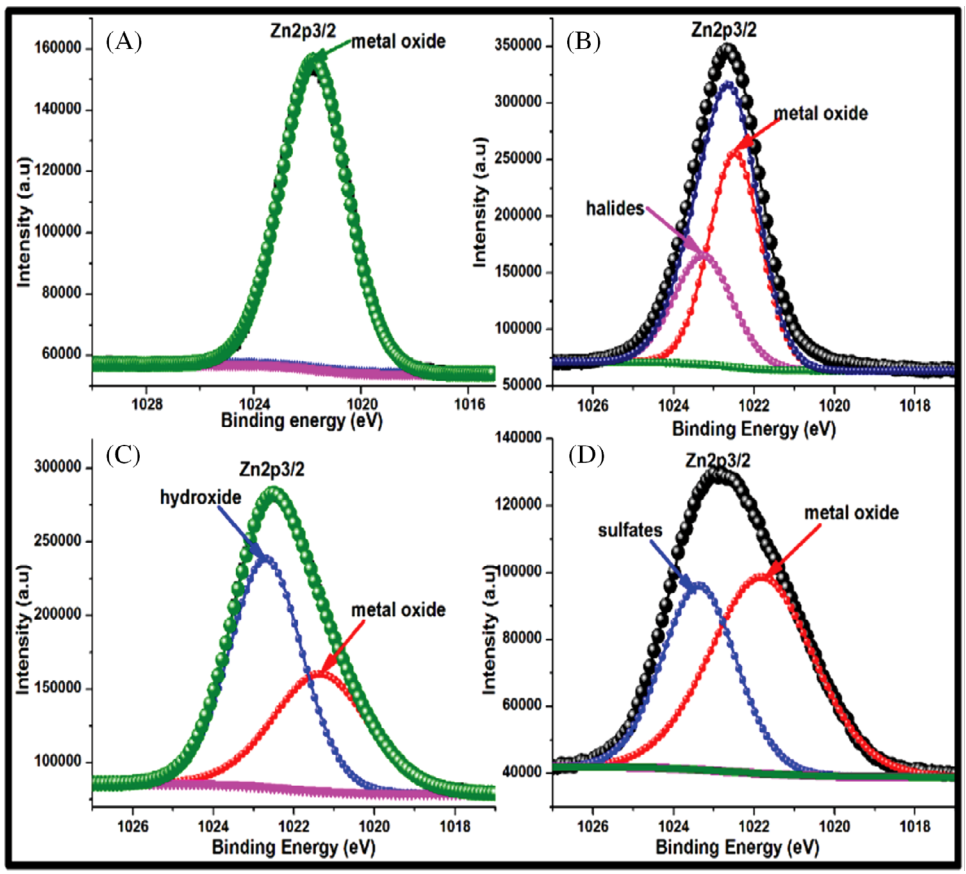

FIGURE 4 X-ray photoelectron spectroscopy (XPS) analysis, Zn $2p_{3/2}$ spectra of the synthesized ZnO samples with (A) Z_a, (B) Z_n, (C) Z_c, and (D) Z_s.

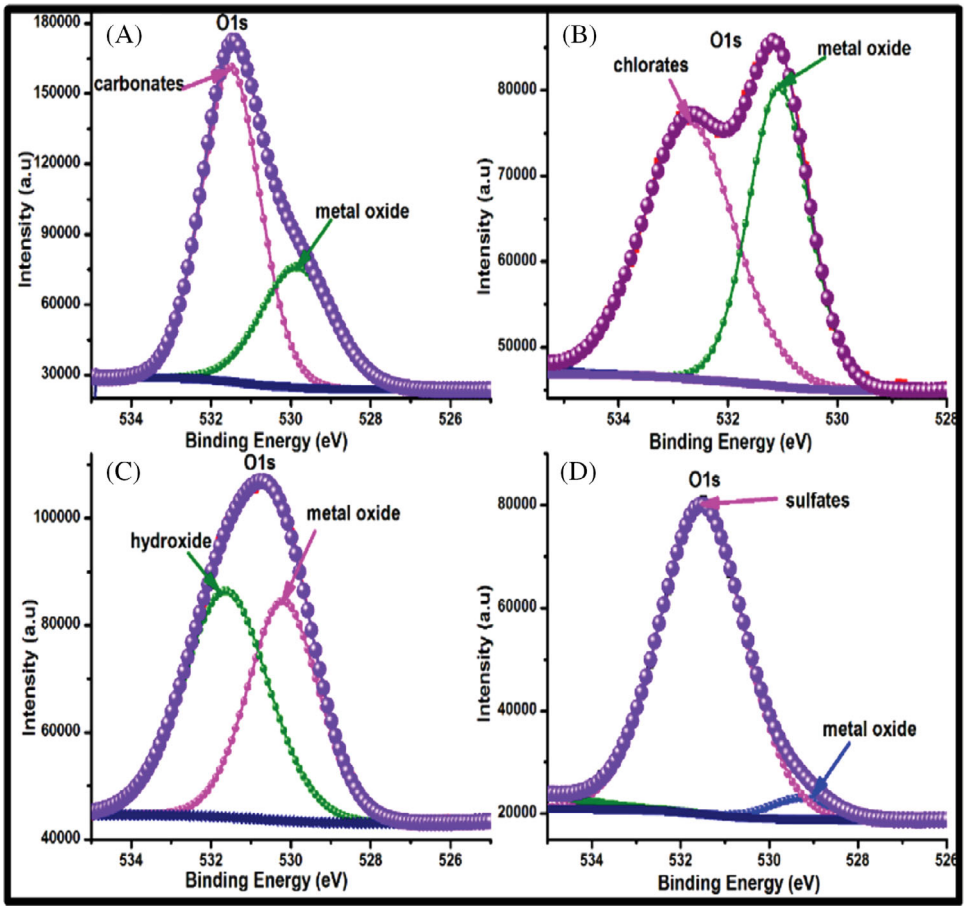

FIGURE 5 X-ray photoelectron spectroscopy (XPS) analysis, O1s spectra of the synthesized ZnO samples with (A) Z_a, (B) Z_n, (C) Z_c, and (D) Z_S.

at 1021.7 eV, a signature min^{-1} of Zn^{2+} in metal oxides, confirming the formation of ZnO in the chemical reaction.[32–34] The O1s peak was deconvoluted into two peaks at 531.5 and 529.8 eV, associated with carbonates or oxygen vacancies[35] and metal oxides,[36,37] respectively. This shows a trace of carbonate from zinc acetate used in the chemical reaction, which can positively or negatively impact the ZnO samples. For the Z_n sample, the Zn $2p_{3/2}$ peak was fitted into two peaks at 1021.4[38,39] and 1022.7 eV,[40] which are associated with metal oxide and hydroxide, respectively. O1s peak was fitted into two peaks at 531.6 and 530.2 eV, which are associated with hydroxides[41] and metal oxides,[42] respectively. This indicates that the annealing process was insufficient to remove all the hydrogen in the sample, leading to the formation of hydroxides. For Z_s samples, the Zn $2p_{3/2}$ peak was fitted into peaks at 1021.8 and 1023.4 eV, which are associated with ZnO[33,34] and $ZnSO_4$ in the sample.[32]

Hence, the ZnO source ($ZnSO_4$) was not wholly precipitated during the chemical reaction. The O1s peak was fitted with two peaks at 531.5 and 529.3 eV, linked with sulfates and metal oxides[43] in the sample. The Zn $2P_{3/2}$ peak was fitted for the Z_c sample with two peaks. The peak at 1022.4 eV is assigned to ZnO,[44] and the halide formed due to the Zn–Cl bond in the sample is represented by the peak at 1023.3 eV.[45] The O1s peak was fitted into two peaks at 532.7 and 531.1 eV, associated with chlorates, chemisorbed oxygen, surface $O.H^-$. groups or dissociated oxygen[46] and metal oxides, respectively. Hence, traces of chlorine from $ZnCl_2$ are still in the ZnO samples.

3.5 | Photocatalytic investigation

The photodegradation activity of the ZnO samples was investigated using the degradation of the model RhB in water in the presence of the samples. The change in concentration C/C_0 as a function of the time of irradiation under UV light is shown in Figure 6A. The decomposition rate of the ZnO samples increases as the time of irradiation increases. At the same time, there is no sign of decomposition of RhB in the absence of ZnO catalysts (denoted as Blank in Figure 6A). It is important to note that the Z_n sample has the best performance up to about 48 min,

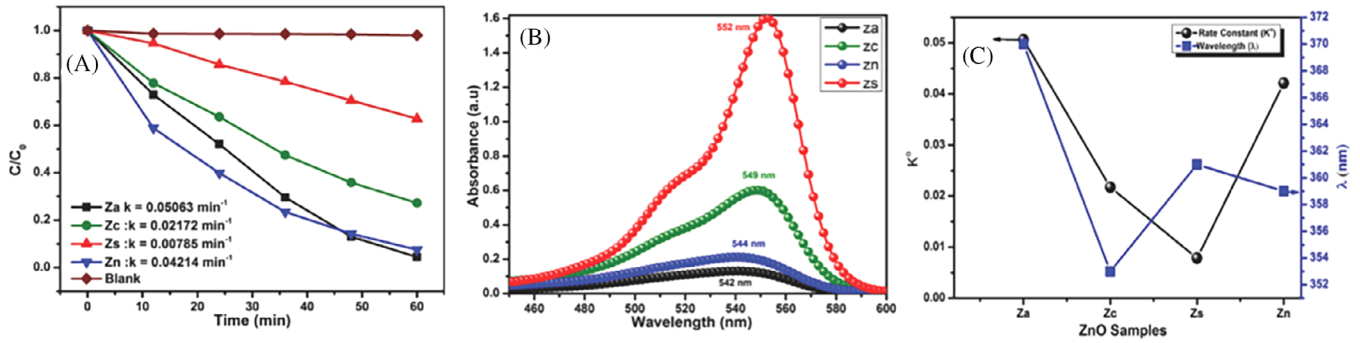

FIGURE 6 (A) Rhodamine B (RhB) degradation activities of samples Z_a, Z_c, Z_s, and Z_n, (B) absorption spectra of RhB solution after 60 min irradiation, and (C) relationship between the absorption edge wavelength and rate constant of the synthesized ZnO samples.

where the efficiency of the photocatalytic degradation of RhB increases in the order of $Z_s < Z_c < Z_a < Z_n$. The sample Z_a has overtaken Z_n in performance at about 48 min. of UV photo-irradiation, and the order of photocatalytic degradation efficiency changes to $Z_s < Z_c < Z_n < Z_a$. The rate constant is obtained by fitting the RhB degradation process using first-order kinetics.[2] A plot of ln(C/Co) against time, which shows they exhibit a linear profile, is used to obtain the rate constant in the bottom left corner of Figure 6A. Z_a sample has the highest value (0.05063 min^{-1}), Z_s has the most negligible value (0.00785 min^{-1}), and the activity decreases in the order $Z_a > Z_n > Z_c > Z_s$. Therefore, Z_a remains the best sample if the rate constant is considered. Further investigation into the degradation rate was done by comparing the absorption spectrum of the samples after 60 min, as shown in Figure 6B, which shows Z_s has the highest absorption intensity and Z_a has the least absorption intensity and the absorption intensity increases in the order $Z_a < Z_n < Z_c < Z_s$. As the amount of RhB that was removed has been estimated by the depreciating absorption curve, Z_a remains the sample with the best photoactivity. The relation between the absorption edge, wavelength, and the rate constant of the zinc oxide samples is shown in Figure 6C. This indicates that the Z_a sample with the highest absorption edge wavelength (370 nm) has the highest rate constant.

3.6 | BET surface area analysis

We have performed the BET experiment on the various samples, and the results are presented in Figure 7A–D, describing the N_2-adsorption and desorption isotherms, showcasing a distinct crossover region where the adsorption and desorption curves intersect. This crossover point indicates a measurement-induced influence on the material under examination. Notwithstanding this effect, utilizing the BET method provides comparative studies on the surface area and pore volume of all the synthesized samples of surface area values from 13.7 to 9.5 m^2/g and corresponding pore volume from 0.05 to 0.03 cm^3/g, particularly calculated from the initial adsorption segment.

Table 1 systematically presents a comprehensive depiction of the BET Method outcomes, encompassing surface area, micropore surface area, cumulative volume, and average pore diameter for a thorough assessment.

Among all synthesized ZnO samples, Z_a stands out for its superior surface area, which indicates the presence of more active adsorption crucial for photocatalysis. This characteristic could enhance Z_a's photocatalytic performance, making it a promising material for such applications.[47]

Remarkably, the findings highlight the superior surface area and large pore size facilitating dye adsorption, thereby improving light harvesting and electrolyte diffusion in the dye-sensitized solar cell exhibited by Z_a relative to the other ZnO precursor powders. This elevation in surface area implies a heightened availability of active adsorption sites, thereby facilitating enhanced photocatalytic performance compared to the alternative ZnO precursor compositions. This heightened activity associated with Z_a is potentially linked to its comparatively smaller average crystallite size than other precursor powder variants, as elucidated in literature sources.[48]

RhB mineralization was quantified through photocatalysis using Equation (1) to determine the extent of mineralization achieved. This equation illustrates the total organic carbon concentrations before and after the photocatalysis reaction. The analysis unveiled that the Z_a sample demonstrated the highest RhB mineralization percentage across the UV light spectrum, consistent with the degradation assessments on RhB. Data about the UV light photocatalysis treatment are visually represented in Figure 8. The notable efficiency of Z_a powder in facilitating substantial mineralization rates under varying light conditions underscores its efficacy, whereas Z_s represents the least

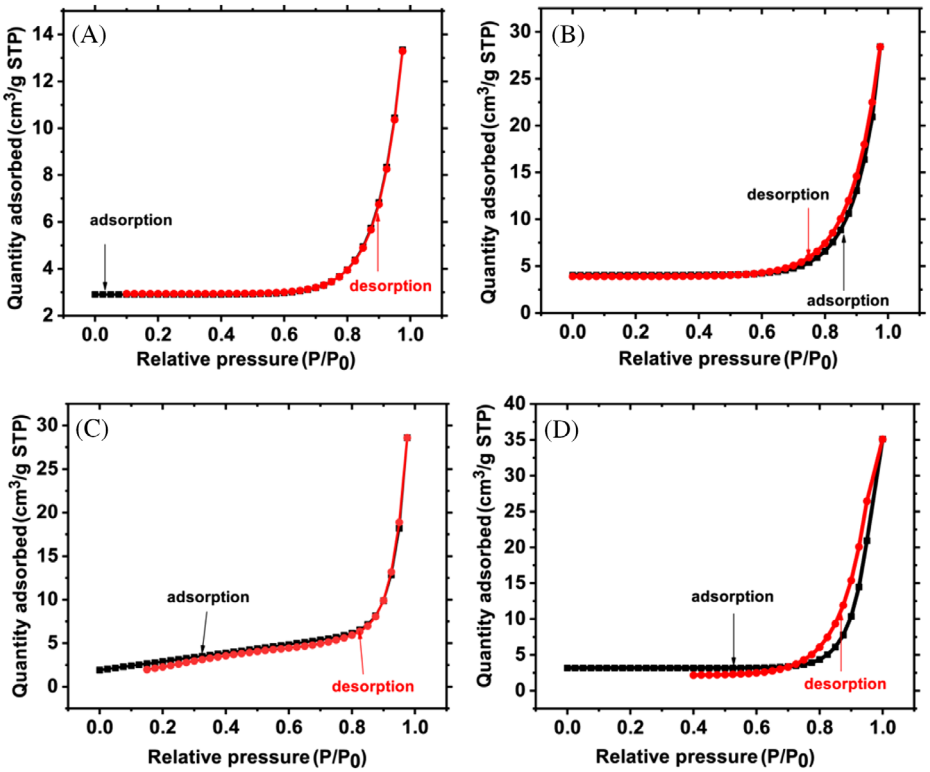

FIGURE 7 N_2-isotherm of all the synthesized samples (A) Z_n, (B) Z_a, (C) Z_c, and (D) Z_s.

TABLE 1 Obtained surface area, micropore surface area, average pore diameter, and pore volume results from the Brunauer–Emmett–Teller (BET) characterization of all the synthesized samples.

Samples	Surface area (m^2/g)	Micropore surface area (m^2/g)	Average pore diameter (nm)	Pore volume (cm^3/g)
Z_s	9.46	7.88	78.83	0.045
Z_n	10.68	2.67	17.36	0.037
Z_c	11.49	2.55	37.02	0.048
Z_a	13.71	1.25	23.68	0.044

mineralization rate.

$$\% \text{ mineralization} = \frac{\text{Change in concentration}}{\text{initial concentration}}. \quad (1)$$

The comparative study of Z_a, Z_n, Z_c, and Z_s photocatalysts for removing RhB dye in an aqueous suspension under UV light illumination has provided valuable insights into their photocatalytic performance. The results show that Z_a exhibited the highest photodegradation efficiency of 97.2%, followed by Z_n at 92.4%, Z_c at 80%, and Z_s at 76% after 60 min of UV light exposure. This indicates that Z_a has the most effective photocatalytic activity among the studied precursors for RhB dye degradation.

Surface properties, particularly in Z_a, have been emphasized as influencing the photocatalytic activity of ZnO precursors. The absorption peak of Z_a in the absorption spectra suggests superior light absorption capabilities compared to the other precursors, which is crucial for initiating photocatalytic reactions.

Z_a's larger surface area and surface defects contribute significantly to its enhanced photocatalytic activity by providing more active sites for the adsorption of organic pollutants. These factors promote the initiation of redox reactions necessary for degrading organic dyes like RhB. Surface defects such as oxygen vacancies enhance charge carrier separation and mobility, which is critical for efficient photocatalysis. The Z_a sample's improved adsorption of organic pollutants promotes efficient interaction between the organic dye and the photocatalyst, facilitating degradation. The redox reactions initiated by Z_a lead to enhanced photocatalytic activity and effective degradation of the RhB dye solution.

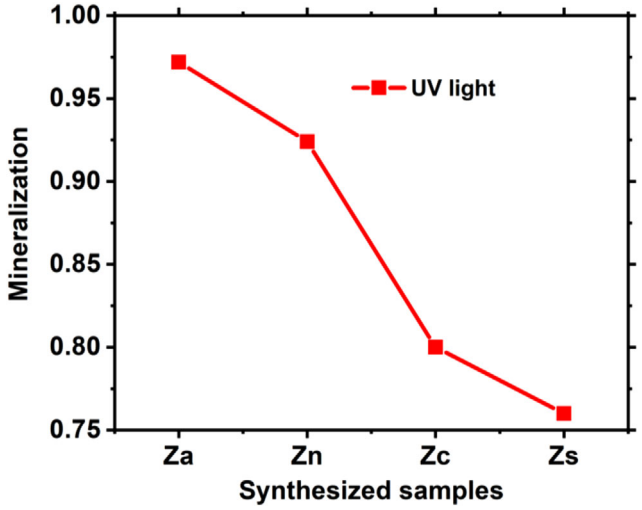

FIGURE 8 All the synthesized ZnO samples were mineralized through total organic carbon analysis after the photocatalytic procedure under UV light conditions.

3.7 | Transient photocurrent and Nyquist impedance analysis

Photocurrent measurements were conducted to assess electron–hole pair separation in all the synthesized ZnO nanoparticles under Xenon arc lamp illumination, leading to photocurrent density values of approximately 5.18, 4.77, 4.15, and 3.69 μAcm^{-2}, for Z_a, Z_c, Z_n and Z_s respectively (Figure 9A).[49]

Sample Z_a demonstrated a significantly higher photocurrent density of 5.18 μAcm^{-2} compared to other synthesized samples, attributed to its enhanced morphology and surface properties contributing to the transient photocurrent enhancement.[50] Further analysis via SEM indicated that Z_a nanoparticles were relatively smaller (approximately 1.12 ± 0.15 nm) than other samples, reinforcing the observed enhancement in photocurrent response. This enhancement led to improved catalyst degradation efficiency in comparison to different samples.

Moreover, electrochemical impedance spectroscopy was employed to investigate the interfacial charge transfer interaction and carrier separation in the synthesized ZnO nanoparticles, with corresponding Nyquist impedance spectra[1] presented in Figure 9B. The smaller arc radius of the Z_a sample, compared to other synthesized ZnO nanoparticles, indicates its superior electron–hole separation capabilities.[51] Combining the results from transient photocurrent, Nyquist impedance spectral analysis, and PL studies confirmed that Z_s demonstrates the least performance. At the same time, Z_a nanoparticles exhibited enhanced electron–hole pair separation, potentially influenced by morphology, inter-band carrier transitions, and the impurity-generated defect factors of the precursors, thereby uniquely influencing the photocatalytic performance.[52] Consequently, Z_a's photocatalytic activity was significantly enhanced.

4 | DISCUSSION

The photodegradation capability of the ZnO samples is affected by several factors, such as optical band gap, crystal defects, structural properties, and morphology. Investigations have been made and reported. Since all these factors are different for the synthesized ZnO samples due to differences in the zinc source, impurity precipitated with these samples will be a significant factor causing the difference in photocatalytic activity. Electrons from the electron–hole pairs generated in the ZnO are transferred from the valence band to the conduction band when the samples are irradiated with UV light because the absorbed photon has energy within the range of the band gap of the semiconductor. This is easier in direct-band

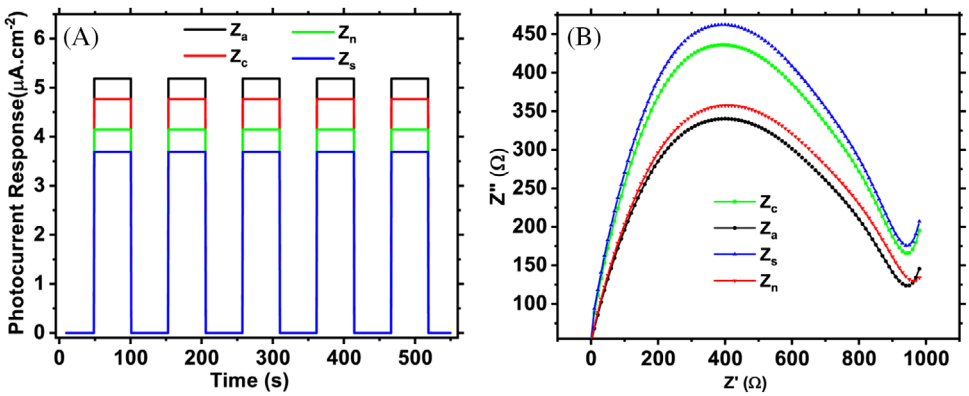

FIGURE 9 (A) Photocurrent response and (B) electrochemical impedance spectroscopy (EIS) Nyquist plot for all the synthesized samples.

gap materials. The separation of electron–hole pairs determines the photocatalytic process because holes generated remove the RhB contaminants in water. Hence, band gap plays a significant role in the performance of the synthesized ZnO samples. As shown in Figure 6A, Z_n and Z_a samples have a competitive effect during the degradation of RhB because Z_a becomes more effective at about 48 min of reaction. This might be due to the indirect band transition associated with Z_n samples. The transition of electrons to the conduction band is assisted by the phonon-generated momentum, which might not be sufficient after 48 min reaction time. The transition of electrons in Z_a is direct; hence, the effectiveness continues after 48 min.

On the other hand, electron–hole recombination is also easier in direct-band gap materials. Photogenerated carriers in defect-free ZnO crystals experience fast surface recombination. However, impurity can hinder this, causing crystal defects in the samples. The crystal defects sometimes improve photocatalytic reaction when they facilitate the separation of photogenerated electron–hole pairs by trapping photogenerated holes that react with electron donors. The visible emission (400–700 nm) observed in the samples' PL spectra suggests that many surface defects exist in the ZnO samples. Hence, surface defects need to be considered one major factor. Notice that the sample Z_a is a direct-band gap material with the best photocatalytic properties. It also has the highest visible emission in the PL result compared to other samples. This means the crystal defect formed in the samples correlates with the photocatalytic activity of the samples.

The enhanced photocatalytic activity of Z_a, attributed to its larger surface area and surface defects, provides more active sites for organic pollutant adsorption, which is crucial for initiating redox reactions that degrade organic dyes like RhB. Surface defects such as oxygen vacancies improve charge carrier separation and mobility, which is essential for efficient photocatalysis. Z_a's increased interaction with organic pollutants effectively facilitates degradation. Z_a exhibited a notably higher photocurrent density of 5.18 μAcm^{-2} compared to other synthesized samples thanks to its superior morphology and surface characteristics that enhance the transient photocurrent. The smaller arc radius of Z_a, reflecting its exceptional electron–hole separation capabilities, outperforms other ZnO nanoparticles. Results from transient photocurrent, Nyquist impedance spectral analysis, and PL studies indicate Z_a's superior electron–hole pair separation, likely influenced by morphology, carrier transitions, and impurity-generated defects in the precursors, all contributing to its exceptional photocatalytic performance. Consequently, Z_a demonstrates significantly improved photocatalytic activity.

5 | CONCLUSIONS

In summary, we explore an in-depth understanding of the photocatalytic properties of ZnO, where an intriguing study was conducted to synthesize four distinct types of nanostructured ZnO samples via precipitation methods, utilizing zinc acetate, zinc nitrate, zinc chloride, and zinc sulfate as precursors. The primary objective was to investigate the efficiency of the synthesized catalysts in degrading the RhB pollutant. The results show that all the as-synthesized ZnO samples exhibited commendable photocatalytic performance. Notably, the ZnO obtained from zinc acetate outperformed the others, demonstrating the highest level of effectiveness. A plethora of advanced analytical techniques are used to comprehensively discuss the underlying factors influencing the performance of the synthesized ZnO catalyst. XRD, XPS, absorption spectrum analysis, SEM, and PL spectroscopy were leveraged to unravel valuable insights into the ZnO samples' properties. The enhanced photocatalytic activity of Z_a's sample, attributed to its larger surface area, surface defects, and superior morphology, excels in organic pollutant degradation. The material's oxygen vacancies improve charge carrier separation, which is crucial for efficient photocatalysis. Again, the interaction with pollutants and high photocurrent density of 5.18 μAcm^{-2} (Z_a) also highlight superior electron–hole pair separation capabilities, influenced by morphology and impurity-generated defects, boosting overall photocatalytic activity significantly.

Hence, this study underscores the significance of careful synthesis and comprehensive characterization in tailoring the properties and optimizing the efficiency of ZnO-based photocatalysts for widespread applications.

ACKNOWLEDGMENTS

This work was supported by the Innovation and Technology Commission of the Hong Kong Special Administrative Region (HKSAR) Government to the Hong Kong Branch of National Rail Transit Electrification and Automation Engineering Technology Research Center under Grant No. K-BBY1.

CONFLICT OF INTEREST STATEMENT

The authors declare no conflicts of interest.

ORCID

Ayodeji Oladiran Awodugba https://orcid.org/0000-0002-6194-5433

REFERENCES

1. Robert D, Piscopo A, Weber JV. Selective solar photodegradation of organopollutant mixtures in water. Sol Energy. 2004;77(5):553–58.

2. Ramírez-Aparicio J, Sánchez-Martínez A, Ramírez-Bon R. Photodecolorization of rhodamine under sunlight irradiation driven by chabazite. Sol Energy. 2016;129:45–53.
3. Wu L, Xing J, Hou Y, Xiao FY, Li Z, Yang HG. Fabrication of regular ZnO/TiO_2 heterojunctions with enhanced photocatalytic properties. Chem–A Eur J. 2013;19(26):8393–96.
4. Mittal M, Sharma M, Pandey OP. UV–visible light-induced photocatalytic studies of Cu doped ZnO nanoparticles prepared by co-precipitation method. Sol Energy. 2014;110:386–97.
5. Zhang X, Qin J, Xue Y, Yu P, Zhang B, Wang L, et al. Effect of aspect ratio and surface defects on the photocatalytic activity of ZnO nanorods. Sci Rep. 2014;4(1):4596.
6. Reynolds DC, Look DC, Jogai B, Collins TC. Polariton and free-exciton-like photoluminescence in ZnO. Appl Phys Lett. 2001;79(23):3794–96.
7. Chandramohan R, Thirumalai J, Vijayan TA, Valanarasu S, Vizhian SE, Srikanth M, et al. Nanocrystalline Mg-doped ZnO dilute magnetic semiconductor prepared by chemical route. Adv Sci Lett. 2010;3(3):319–22.
8. Pardeshi SK, Patil AB. A simple route for photocatalytic degradation of phenol in aqueous zinc oxide suspension using solar energy. Sol Energy. 2008;82(8):700–705.
9. Gumus CE, Ozkendir OM, Kavak H, Ufuktepe YÜ. Structural and optical properties of zinc oxide thin films prepared by spray pyrolysis method. J Optoelectron Adv Mater. 2006;8(1):299–303.
10. Ni YH, Wei XW, Hong JM, Ye Y. Hydrothermal preparation and optical properties of ZnO nanorods. Mater Sci Eng: B. 2005;121(1–2):42–47.
11. Scarisoreanu N, Matei DG, Dinescu G, Epurescu G, Ghica C, Nistor LC, et al. Properties of ZnO thin films prepared by radio-frequency plasma beam assisted laser ablation. Appl Surf Sci. 2005;247(1–4):518–25.
12. Ristić M, Musić S, Ivanda M, Popović S. Sol–gel synthesis and characterization of nanocrystalline ZnO powders. J Alloys Compd. 2005;397(1–2):1–4.
13. Chang SS, Yoon SO, Park HJ, Sakai A. Luminescence properties of Zn nanowires prepared by electrochemical etching. Mater Lett. 2002;53(6):432–36.
14. Wu JJ, Liu SC. Low-temperature growth of well-aligned ZnO nanorods by chemical vapour deposition. Adv Mater. 2002;14(3):215–18.
15. Lin CS, Hwang CC, Lee WH, Tong WY. Preparation of zinc oxide (ZnO) powders with different types of morphology by a combustion synthesis method. Mater Sci Eng: B. 2007;140(1–2):31–37.
16. Hwang CC, Wu TY. Synthesis and characterization of nanocrystalline ZnO powders by a novel combustion synthesis method. Mater Sci Eng: B. 2004;111(2–3):197–206.
17. Wang RC, Tsai CC. Efficient synthesis of ZnO nanoparticles, nanowalls, and nanowires by thermal decomposition of zinc acetate at a low temperature. Appl Phys A. 2009;94:241–45.
18. Singh O, Kohli N, Singh RC. Precursor controlled morphology of zinc oxide and its sensing behaviour. Sens Actuators, B. 2013;178:149–54.
19. Zak AK, Abd Majid WH, Wang HZ, Yousefi R, Golsheikh AM, Ren ZF. Sonochemical synthesis of hierarchical ZnO nanostructures. Ultrason Sonochem. 2013;20(1):395–400.
20. Rajesh D, Lakshmi BV, Sunandana CS. Two-step synthesis and characterization of ZnO nanoparticles. Physica B. 2012;407(23):4537–39.
21. Bilecka I, Elser P, Niederberger M. Kinetic and thermodynamic aspects in the microwave-assisted synthesis of ZnO nanoparticles in benzyl alcohol. ACS Nano. 2009;3(2):467–77.
22. Hong R, Pan T, Qian J, Li H. Synthesis and surface modification of ZnO nanoparticles. Chem Eng J. 2006;119(2–3):71–81.
23. Tseng CC, Chou YH, Liu CM, Liu YM, Ger MD, Shu YY. Microwave-assisted hydrothermal synthesis of zinc oxide particles starting from chloride precursor. Mater Res Bull. 2012;47(1):96–100.
24. Wahab R, Kim YS, Shin HS. Synthesis, characterization and effect of pH variation on zinc oxide nanostructures. Mater Trans. 2009;50(8):2092–97.
25. Thirumavalavan M, Huang KL, Lee JF. Preparation and morphology studies of nano zinc oxide obtained using native and modified chitosans. Materials. 2013;6(9):4198–212.
26. Sharma D, Sharma S, Kaith BS, Rajput J, Kaur M. Synthesis of ZnO nanoparticles using surfactant-free in-air and microwave method. Appl Surf Sci. 2011;257(22):9661–72.
27. Seifikar F, Habibi-Yangjeh A. Floating photocatalysts as promising materials for environmental detoxification and energy production: a review. Chemosphere. 2024;355:141686.
28. Habibi-Yangjeh AKP. A review on emerging homojunction photocatalysts with impressive performances for wastewater detoxification. Crit Rev Environ Sci Technol. 2024;54(4):290–320.
29. Hemmati-Eslamlu P, Habibi-Yangjeh A. A review of impressive Z- and S-scheme photocatalysts composed of g-C_3N_4 for detoxification of antibiotics. FlatChem. 2024;43:100597.
30. Ma W, Ma R, Liang J, Wang C, Liu X, Zhou K, et al. Layered zinc hydroxide nanocones: synthesis, facile morphological and structural modification, and properties. Nanoscale. 2014;6(22):13870–75.
31. Bindu P, Thomas S. Estimation of lattice strain in ZnO nanoparticles: x-ray peak profile analysis. J Theor Appl Phys. 2014;8:123–34.
32. Fadley CS. X-ray photoelectron spectroscopy: progress and perspectives. J Electron Spectrosc Relat Phenom. 2010;178–179:2–32.
33. Ramgir NS, Late DJ, Bhise AB, More MA, Mulla IS, Joag DS, et al. ZnO multipods, submicron wires, spherical structures and their unique field emission behaviour. J Phys Chem B. 2006;110(37):18236–42.
34. Zheng JH, Jiang Q, Lian JS. Synthesis and optical properties of flower-like ZnO nanorods by thermal evaporation method. Appl Surf Sci. 2011;257(11):5083–87.
35. Hsieh PT, Chen YC, Kao KS, Wang CM. Luminescence mechanism of ZnO thin film investigated by XPS measurement. Appl Phys A. 2008;90:317–21.
36. Al-Gaashani R, Radiman S, Daud AR, Tabet N, Al-Douri YJ. XPS and optical studies of different morphologies of ZnO nanostructures prepared by microwave methods. Ceram Int. 2013;39(3):2283–92.
37. Feng L, Liu A, Liu M, Ma Y, Wei J, Man B. Synthesis, characterization and optical properties of flower-like ZnO nanorods by non-catalytic thermal evaporation. J Alloys Compd. 2010;492(1–2):427–32.
38. Du Y, Zhang MS, Hong J, Shen Y, Chen Q, Yin Z. Structural and optical properties of nanophase zinc oxide. Appl Phys A. 2003;76:171–76.

39. Karamat S, Rawat RS, Lee P, Tan TL, Ramanujan RV. Structural, elemental, optical and magnetic study of Fe doped ZnO and impurity phase formation. Prog Nat Sci: Mater Int. 2014;24(2):142–49.
40. Popescu AM, Neacşu EI, Yanushkevich K, Constantin V. Surface analysis and corrosion resistance of new nickel base thin film alloys. Surf Interface Anal. 2014;46(6):378–86.
41. Platzman I, Saguy C, Brener R, Tannenbaum R, Haick H. Formation of ultrasmooth and highly stable copper surfaces through annealing and self-assembly of organic monolayers. Langmuir. 2010;26(1):191–201.
42. Lee J, Chung J, Lim S. Improvement of optical properties of post-annealed ZnO nanorods. Physica E. 2010;42(8):2143–46.
43. Das J, Pradhan SK, Sahu DR, Mishra DK, Sarangi SN, Nayak BB, et al. Micro-Raman and XPS studies of pure ZnO ceramics. Physica B. 2010;405(10):2492–97.
44. Zhang J, Gao D, Yang G, Zhang J, Shi Z, Zhang Z, et al. Synthesis and magnetic properties of Zr doped ZnO Nanoparticles. Nanoscale Res Lett. 2011;6:1–7.
45. Yu Y, Wang J, Li W, Zheng W, Cao Y. Doping mechanism of Zn 2+ ions in Zn-doped TiO 2 prepared by a sol-gel method. CrystEngComm. 2015;17(27):5074–80.
46. Bang S, Lee S, Ko Y, Park J, Shin S, Seo H, et al. Photocurrent detection of chemically tuned hierarchical ZnO nanostructures grown on seed layers formed by atomic layer deposition. Nanoscale Res Lett. 2012;7(1):290.
47. Lundstedt C. BET Theory and how its used to calculate surface area. Kyoto: HORIBA Scientific; 2019.
48. Wang X, Chang R, Ding Y, Zhou B, Cao Q, Bi H. Characterization of the average pore diameter of nanoporous media by gas permeability measurement technique in transitional flow regime. Vacuum. 2021;194:110596.
49. Zhang G, Ge T, Zhang Y, Zhang E, Ma H, Hou J. Hydrothermal preparation of Nb^{5+}-doped α-Fe_2O_3 nanorods for efficient visible-light-driven photocatalytic reduction of hexavalent chromium. Powder Technol. 2024;436:119480.
50. Dou Q, Hou J, Hussain A, Zhang G, Zhang Y, Luo M, et al. One-pot synthesis of sodium-doped willow-shaped graphitic carbon nitride for improved photocatalytic activity under visible-light irradiation. J Colloid Interface Sci. 2022;624:79–87.
51. Zhang Y, Liu C, Nian P, Ma H, Hou J, Zhang Y. Facile preparation of high-performance hydrochar/TiO_2 heterojunction visible light photocatalyst for treating Cr(VI)-polluted water. Colloids Surf A Physicochem Eng Asp. 2024;681:132775.
52. Kumaresan N, Maria Angelin Sinthiya M, Praveen Kumar M, Ravichandran S, Ramesh Babu R, Sethuramanet K, et al. Investigation on the photocatalytic and sonophotocatalytic activities of {002} facets of ZnO nanoparticles synthesized through template/surfactant-free hydrothermal method at different temperatures and time durations. J Mater Sci Mater Electron. 2020;31(16):13817–37.

How to cite this article: Ilyas AM, Musah J-D, Or SW, Awodugba AO. Precursor impurity-mediated effect in the photocatalytic activity of precipitated zinc oxide. J Am Ceram Soc. 2024;107:8269–80. https://doi.org/10.1111/jace.20062